Supplementary Materials: In-Situ Synthesis of Nb_2O_5/g-C_3N_4 Heterostructures as Highly Efficient Photocatalysts for Molecular H_2 Evolution under Solar Illumination

Faryal Idrees, Ralf Dillert, Detlef Bahnemann, Faheem .K. Butt and Muhammad Tahir

Type-II and Z-Scheme Schematic

More precisely, the higher conduction band (CB) of one photocatalyst contribute to the reduction reactions and lower valence band (VB) of the second photocatalyst to the oxidation reactions. While the electron mediators (such as noble metals Pt, Au, and Ag) would provide an interface through which the photogenerated electrons of lower CB of one photocatalyst and photogenerated holes of higher VB of another photocatalyst could recombine quickly, leaving more reductive electrons and more oxidative holes at corresponding active sites. According to schematic after coming into contact, the electrons will flow from high Fermi level semiconductor to the low Fermi level semiconductor until their Fermi levels align at the same level. This equilibrium develops an electric field at the interface due to positive and negative charges developed at the semiconductors surfaces, respectively. The electrons can move quickly towards downward band bending and holes towards upward band bending, forbidding their contrary bending, respectively. Therefore, in the direct Z-scheme, the interfacial electrons and holes undergo a recombination process, following the reduction and oxidation at different semiconductors bands. [a–d]

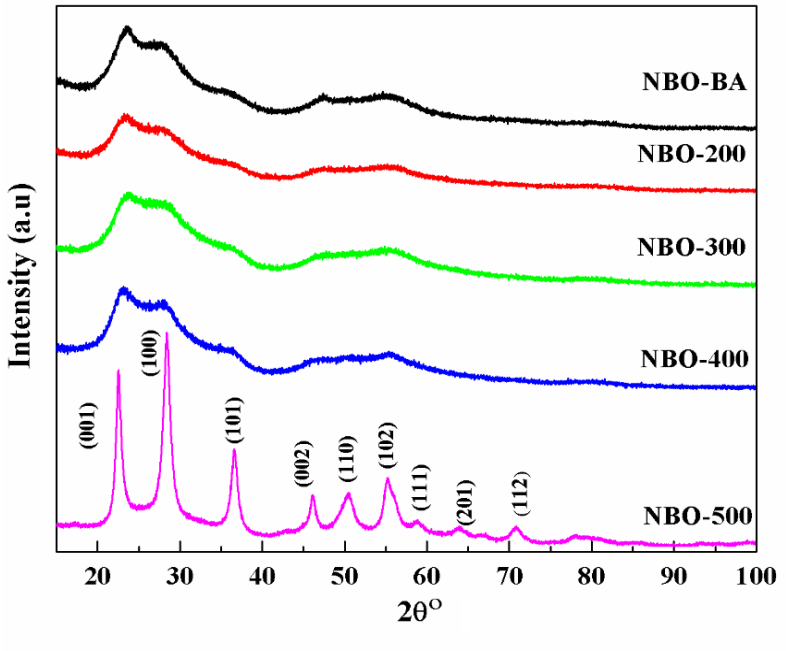

Figure S1. XRD patterns BA and AA at different calcination temperatures.

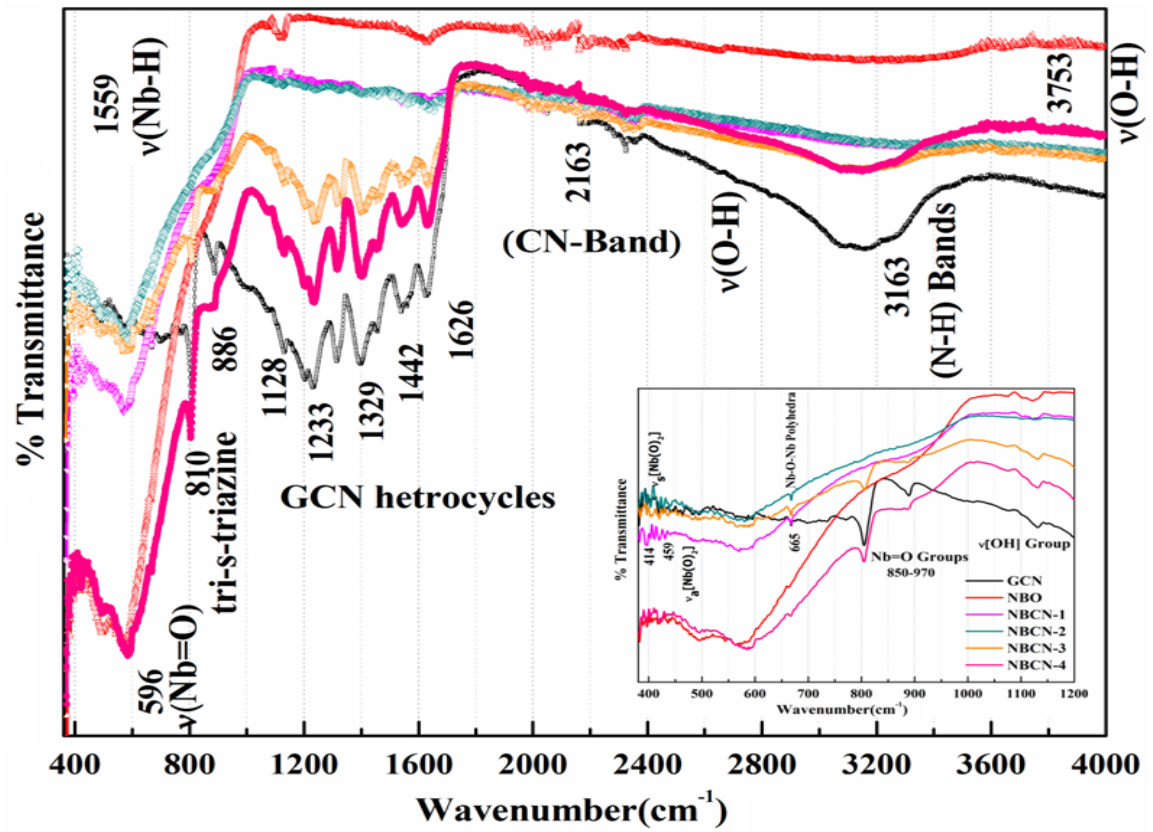

Figure S2. FTIR spectra of all photocatalysts.

Table S1. Associated Bands in FTIR Spectra.

Wavenumber(cm^{-1})	Band	Wavenumber(cm^{-1})	Band
810	characteristic of tri-s-triazine	1242-1637	stretching modes of CN heterocycles
3163(Broad)	N-H bands(bulk GCN) Presence of NH_2 and NH bands and absence of an H_2 bond	2163	C-N band stretching vibration modes
1200-1650	Several bands CN heterocycles		
3410,1635(3745)	vibration of OH v(O-H) groups	640	stretching vibration of Nb–O–Nb
953	Nb-O	414	$v_s[Nb(O)_2]$
459 cm^{-1}	$v_a[Nb(O)_2]$	665	v(Nb-O-Nb)
850-970	v(Nb=O)		

Table S2. Specific surface area (m^2/g) of samples with different calcination temperatures.

Calcination Temp.	BA	200	300	400	500
NBCN-2	227	212	199	178	50
NBO	250	237	202	183	58
GCN	9	-	-	-	-
NBCN-1	220	-	-	-	-
NBCN-3	215	-	-	-	-
NBCN-4	159	-	-	-	-

Table S3. Specific surface area of NBO and NBCN-X (X=1-4) without calcination.

Samples	NBO-BA	NBO	NBCN-1	NBCN-2	NBCN-3	NBCN-4	GCN
Specific Surface Area (m^2g^{-1})	250	237	220	227	216	159	9

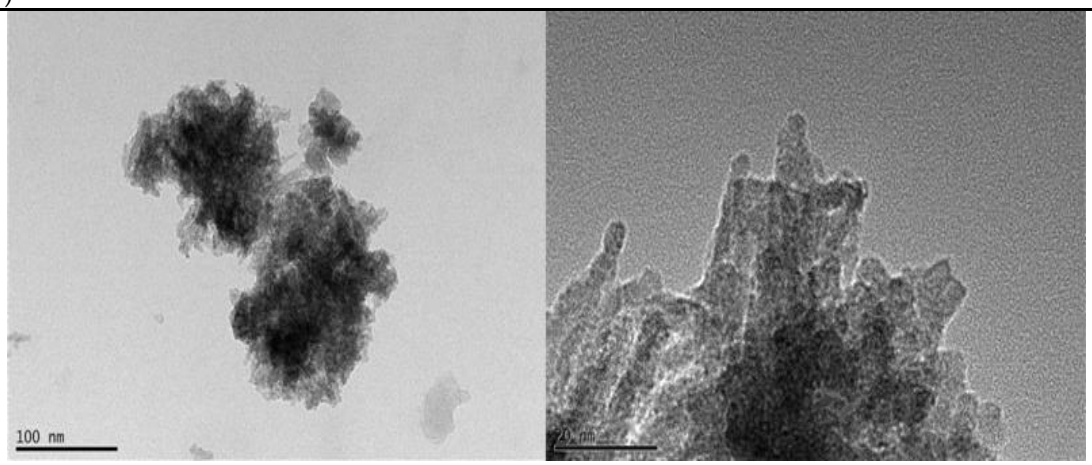

Figure S3. TEM images of NBO.

UV-vis-Diffuse Absorption Spectra

We measured the optical absorption spectrum of as-synthesized samples of NBO, GCN, and NBCN-X (X=1-4) to determine their energy bandgaps. Since the amorphous materials have an indirect bandgap, so we calculated the indirect bandgaps for all photocatalysts by using a typical calculation. Bandgap $E(eV) = h\nu$, where h = Planck's constant, $\nu = c/\lambda$ with c = speed of light and λ= wavelength corresponds to α = absorption coefficient of Tauc's plot. Thus, plots between the value of $E(eV)$ on the horizontal axis and $(\alpha h\upsilon)^{1/2}$ have drawn and estimated by linear extrapolation to the x-axis. The estimated bandgaps for NBO = 3.01 eV, GCN = 2.56 eV and NBCN-X (X=1,2,3,4) = 2.95, 2.70, 2.60, 2.50 eV, respectively. All the composites bandgaps have been reduced to the visible region. A continuous redshift has been observed with the increasing ratio of GCN, as shown in S7 (a). The change in the bandgaps according to post-calcination temperature has also been estimated (provided in S7 (b). No significant change has been observed with the increase in the calcination temperature, which indicates that the photocatalytic properties have been associated more with the structural properties than the bandgap.

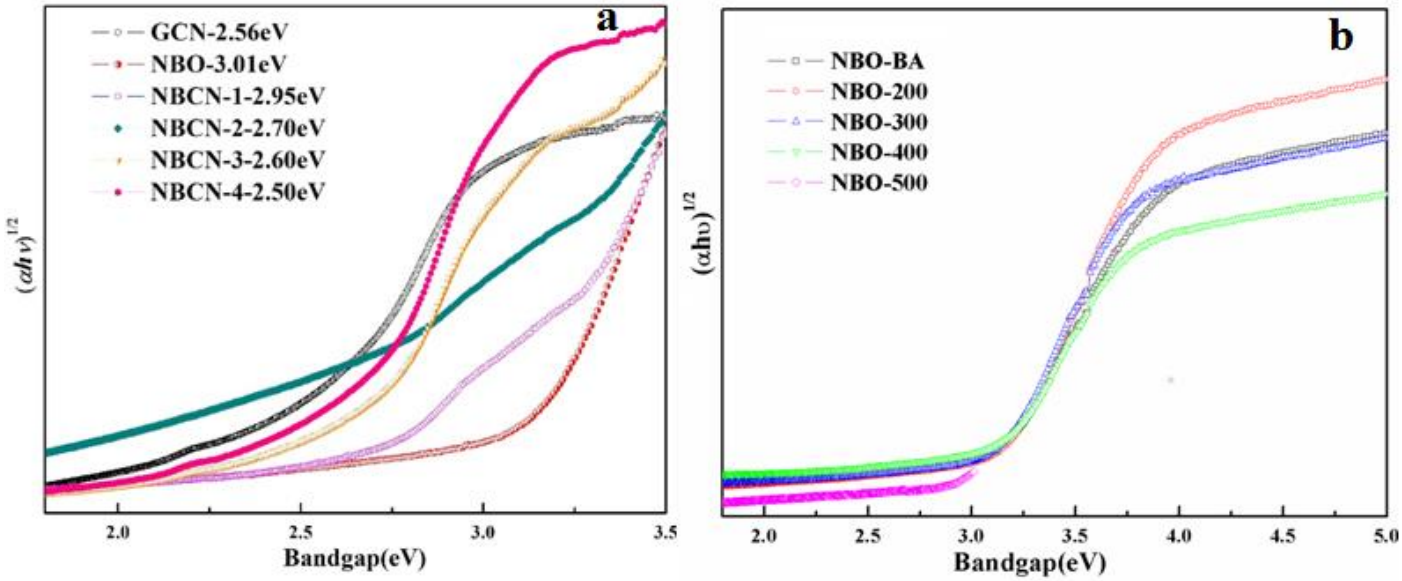

Figure S4. Bandgap vs photon energy by UV-vis-Diffuse Absorption Spectra of a) NBO, GCN, NBCN-1, NBCN-2, NBCN-3, and NBCN-4 and b) with the change in the annealing temperature.

Physical Mixing

The efficiency of the proposed method for obtaining heterojunctions was compared by preparing a physical mixture of g-C_3N_4 and as-prepared Nb_2O_5 by simple grinding in an agate mortar for 30 min. The material was obtained using a 0.03 g of g-C_3N_4 and a 0.25 g of Nb_2O_5.

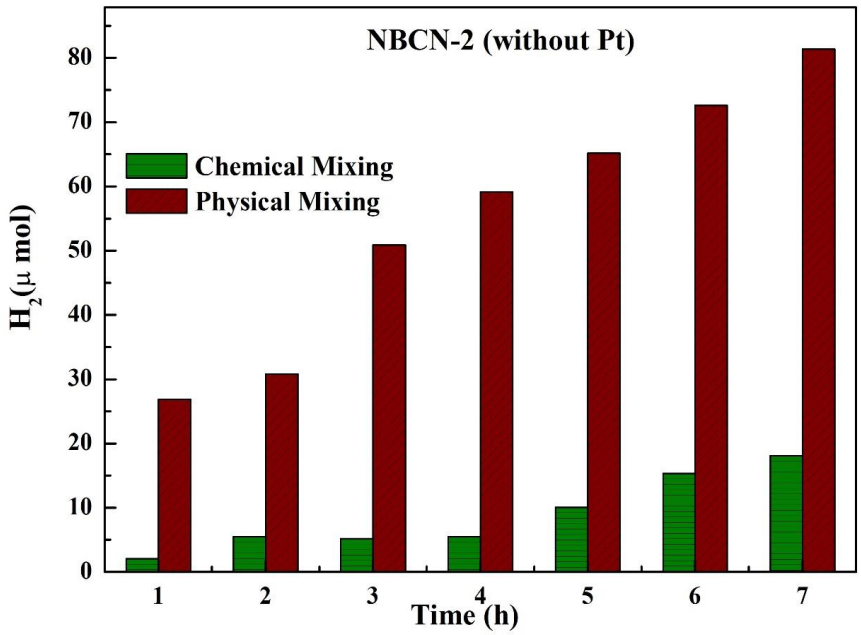

Figure S5. Molecular H_2 generation of NBCN-2, Chemical and Physical Mixing in the presence of methanol.

Table S4. Liberated Amount of H_2 after 7h with and without Pt.

		Photocatalyst	With Pt (mmol)	Without Pt (mmol)
With Metha-nol	With TEOA	P25	3.18	0.64
		NBO	2.88	0.33
		GCN	2.34	0.11
		NBCN-1	7.23	1.00
		NBCN-2	7.7	1.95
		NBCN-3	5.10	0.86
		NBCN-4	3.92	0.79
		NBCN-2-Physical Mixing	---	0.06
		NBCN-2	0.61	0.36

Photoelectrochemical Conversions

$$V_{CB} \approx V_{FB(NHE,pH\ 7)} = V_{FB\left(\frac{Ag}{AgCl},pH\ 5.6\right)} - 0.059(7-5.6) \quad \text{Equation S1}$$

$$V_{VB} = V_{CB} + \frac{E_g}{e} \quad \text{Equation S2}$$

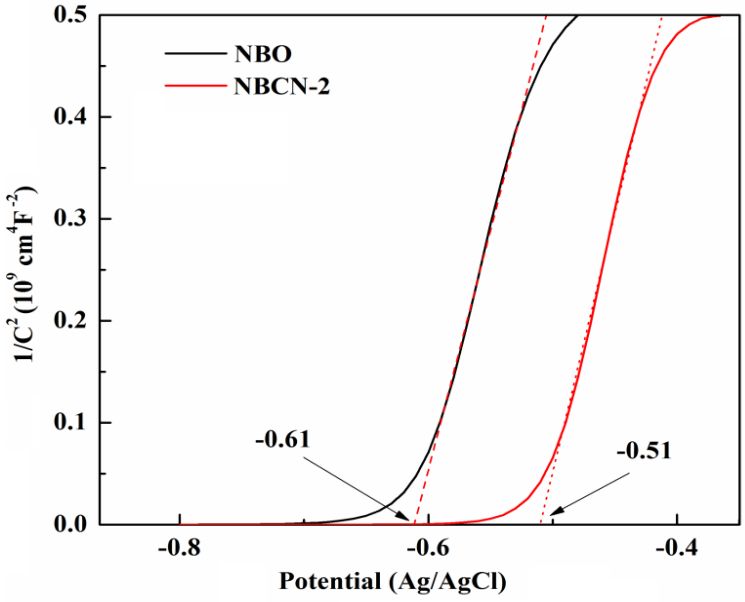

Figure S6. Mott-Schottky plot of NBO and NBCN-2.

a. Hong, Y., et al., *Efficient and stable Nb2O5 modified g-C3N4 photocatalyst for removal of antibiotic pollutant.* Chemical Engineering Journal, 2016. **299**(Supplement C): p. 74-84.

b. Huang, Q.-Z., et al., *In-situ growth of mesoporous Nb2O5 microspheres on g-C3N4 nanosheets for enhanced photocatalytic H2 evolution under visible light irradiation.* International Journal of Hydrogen Energy, 2017. **42**(10): p. 6683-6694.

c. Low, J., et al., *A Review of Direct Z-Scheme Photocatalysts.* Small Methods, 2017.

d. Huang, Z.-F., et al., *Switching charge transfer of C3N4/W18O49 from type-II to Z-scheme by interfacial band bending for highly efficient photocatalytic hydrogen evolution.* Nano Energy, 2017. **40**: p. 308-316.